Article

Simultaneous enhancement of strength and ductility *via* microband formation and nanotwinning in an L1$_2$-strengthened alloy

Lu Yang [a], Dingshan Liang [a], Zhuo Cheng [a], Ranxi Duan [a], Chuanxin Zhong [a], Junhua Luan [b], Zengbao Jiao [c], Fuzeng Ren [a],[*]

[a] Department of Materials Science and Engineering, Southern University of Science and Technology, Shenzhen 518055, China
[b] Department of Materials Science and Engineering, City University of Hong Kong, Hong Kong 999077, China
[c] Department of Mechanical Engineering, The Hong Kong Polytechnic University, Hong Kong 999077, China

ARTICLE INFO

ABSTRACT

Metallic alloys with high strength and large ductility are required for extreme structural applications. However, the achievement of ultrahigh strength often results in a substantially decreased ductility. Here, we report a strategy to achieve the strength-ductility synergy by tailoring the alloy composition to control the local stacking fault energy (SFE) of the face-centered-cubic (fcc) matrix in an L1$_2$-strengthened superlattice alloy. As a proof of concept, based on the thermodynamic calculations, we developed a non-equiatomic CoCrNi$_2$(Al$_{0.2}$Nb$_{0.2}$) alloy using phase separation to create a near-equiatomic low SFE disordered CoCrNi medium-entropy alloy matrix with *in situ* formed high-content coherent Ni$_3$(Al, Nb)-type ordered nanoprecipitates ($\sim$ 12 nm). The alloy achieves a high tensile strength up to 1.6 GPa and a uniform ductility of 33%. The low SFE of the fcc matrix promotes the formation of nanotwins and parallel microbands during plastic deformation which could remarkably enhance the strain hardening capacity. This work provides a strategy for developing ultrahigh-strength alloys with large uniform ductility.

1. Introduction

The production of high-performance alloys with gigapascal strength and large ductility has been the research focus of materials scientists and engineers. However, in most alloys, strength and ductility are generally mutually exclusive: increasing strength often requires striking a compromise with ductility, leading to a strength-ductility trade-off [1]. Resolving this dilemma is an important challenge in materials science. In recent years, significant progress has been made in achieving strength-ductility combinations which give mechanical properties superior to those of conventional microstructures by engineering the internal grain structures, *e.g.* by forming bimodal [2], lamellar [3], gradient [4], and hierarchical nanostructures [5]. However, obtaining ultra-high yield strength of > 1 GPa and large uniform tensile ductility of > 20% for extreme structural applications remains a grand challenge [6].

Recently, high-entropy alloys (HEAs) with multi-principal elements greatly enrich the design space of alloy composition. The high configurational entropy promotes the formation of disordered single-phase solid solution structure by the reduction in Gibbs free energy of mixing, such as face-centered cubic (fcc), body-centered cubic (bcc), and hexagonal close-packed (hcp) [7–10]. Among these HEAs, the fcc HEAs

have drawn particular attention owing to their outstanding ductility [11] and fracture toughness especially at cryogenic temperatures [12]. Extensive research efforts have been devoted to the underlying deformation mechanisms of these alloys and thus various strain-hardening mechanisms have been reported, namely, transformation-induced plasticity (TRIP) [13], twinning-induced plasticity (TWIP) [14] and microband-induced plasticity (MBIP) [15,16]. Activation of the dominant deformation mechanism in fcc alloys largely depends on their stacking fault energy (SFE) [17]. At low SFE (< 20 mJ/m^2), phase transformation can be activated, which results in TRIP effect. The TWIP effect operates predominantly in medium-SFE alloys (20-40 mJ/m^2). The recently proposed MBIP mechanism in high-SFE alloys (> 50 mJ/m^2) involves the formation of narrow planar shear zones, which are delimited by geometrically necessary boundaries [18–20]. All these mechanisms result in strong grain subdivision or microstructure refinement during straining, and thus lead to high strain-hardening rates (SHRs). For example, the deformation in fcc quinary CoCrFeMnNi and quaternary CoCrFeNi HEAs is dominated by dislocation activities at room temperature. These HEAs show extensive twinning at cryogenic temperatures because of the decrease in the SFE and increase in the thermally activated Peierls stress for dislocation motion with decreasing temperature. However, deformation twins are difficult to form in uniaxial tension at room tem-

---

[*] Corresponding author.
E-mail address: renfz@sustech.edu.cn (F. Ren).

perature due to the fact that the resolved shear stress is insufficient to overcome the critical stress for twinning [21,22]. Furthermore, for a typical fcc medium-entropy alloy (MEA) CoCrNi, its low SFE promotes the perfect dislocations to dissociate into $a/6\langle112\rangle$ partial dislocations at relatively low strains. Then further deformation leads to the formation of nanotwins and hcp lamellae which act as barriers to dislocation motion at room temperature and thus increase the SHR and strength-ductility compared with those of a CoCrFeMnNi HEA [23,24]. Note that fcc alloys usually have relatively low yield strength (< 0.6 GPa) at room temperature [25,26]. The recently developed $L1_2$ precipitation-strengthened fcc HEAs have shown great potential for achieving ultrahigh strength with good ductility by generating distinctive multistage strain-hardening behavior, as a result of pronounced dislocation activities and deformation-induced microbands [16,27-30]. However, high-density stacking faults (SFs) rather than deformation twins were present, even under high strains at 77 K [31]. Therefore, tuning SFE in fcc alloys together with $L1_2$ precipitation strengthening would be a promising route to fabricate advanced alloys with high strength, large ductility and large SHR.

SFE is a critical parameter in plastic deformation, dislocation mobility, deformation twinning, and initiation of phase transformation. In conventional alloys, SFE is almost constant throughout the material. However, in HEAs, the SFE can vary locally, even with lattice and local chemical ordering. This affects the dissociation behavior of dislocations and, in turn, the bulk deformation behavior [32,33]. This raises two interesting questions: (i) can TWIP and MBIP be simultaneously achieved in $L1_2$-strengthened HEAs by tailoring the chemical composition of the fcc matrix to control the local SFE of alloy? (ii) can the SHR be increased *via* the formation of nanotwins and microbands in $L1_2$-strengthened HEAs? Motivated by these questions and in an attempt to address the strength-ductility trade-off, we designed a novel $CoCrNi_2(Al_{0.2}Nb_{0.2})$ alloy by a computational thermodynamic approach. The formation of a low SFE matrix in the as-aged alloy can activate the formation of deformation-induced nanotwins and parallel microbands which further improve the strain-hardening ability and enable large ductility to be achieved at a gigapascal stress level. The aged alloy exhibited ultrahigh yield and tensile strengths of 1.15 and 1.6 GPa, respectively, combined with a large uniform ductility of 33%. Our results show that tailoring the alloy composition to control the local SFE of the fcc matrix in $L1_2$-strengthened alloys provides a promising design concept for achieving an excellent combination of high strength and large uniform ductility in HEAs.

2. Computational and experimental procedures

2.1. Thermodynamic calculations using CALPHAD

Increasing the Ni concentration in the $L1_2$-strengthened fcc CoCrNi based M/HEAs will greatly increase the content of $L1_2$ phase and the space for alloy design. In view of this, the $CoCrNi_2$ was used as the base alloy in the present work while Al and Nb elements were added to induce precipitation hardening. The CALPHAD (CALculation of PHAse Diagrams) was used to predict the change in the fcc + $L1_2$ two phase region by varying the Al content in the alloy. Simulations were performed using the Thermo-Calc Software Version 2019a with a Ni-based database (TTNI8). The optimized composition to increase the $L1_2$ phase stability and volume fraction is located at $CoCrNi_2(Al_{0.2}Nb_{0.2})$.

2.2. Sample preparation

Non-equiatomic $CoCrNi_2(Al_{0.2}Nb_{0.2})$ alloy ingots were prepared by electromagnetic levitation melting under high-purity argon atmosphere. All the raw pure metals have purities of ≥ 99.9 wt.%. A 3 kg cast of this alloy was produced and cast into ingots with a diameter of 110 mm and a height of 100 mm. To chemically homogenize the as-cast alloy and decrease the elemental segregation, the ingots were solution-treated for

24 h at 1200 °C and followed by water quenching. The solution-treated alloys (80 mm × 20 mm × 5 mm) were then cold-rolled along the length direction at room temperature with a thickness reduction of 70% from 5 mm to 1.5 mm by 6 passes. The cold-rolled sheets were recrystallized at 1050 °C for 10 min to control the grain size. The samples were duplex-aged at 720 °C for 8 h and 620 °C for 8 h, and then quenched in water.

2.2. Mechanical tests

Dog-bone-shaped specimens for tensile tests with a gauge length of 12.5 mm were cut from the aged sheets using an electrical discharge machine. The gauge sections were then mechanically ground using SiC paper. Tensile tests at room temperature were conducted using a universal testing machine (CMT5105, MTS, China) with a strain rate of 1×10^{-3} s^{-1}. All tensile tests were carried out with a 10-mm-gauge extensometer attached to the gauge section to monitor the engineering strain. Three independent tests were performed to confirm the reproducibility.

2.3. Microstructural and compositional characterization

X-ray diffraction (XRD) pattern of the aged alloy was recorded using a Smartlab-9 kW diffractometer (Rigaku, Japan) in the 2θ range of 20°–100° with Cu $K\alpha$ radiation (λ = 1.54056 Å, 45 kV, 200 mA). The microstructure was examined by scanning electron microscopy (SEM; MIRA 3, TESCAN, Czech Republic) along with energy dispersive X-ray spectroscopy (EDX). Grain morphology, orientation and size of the alloy were analyzed using electron back-scattering diffraction (EBSD; Nordlys Max², Oxford Instruments plc, Oxford, UK) equipped with SEM. The EBSD specimens were first mechanically polished using SiC paper down to 1200 grit and then subjected to vibrational polishing (Buehler Vibromet 2) in a colloidal silica (0.05 μm) suspension for 12 h. The microstructure of the as-aged alloy was also investigated by transmission electron microscopy (TEM) and high-resolution TEM (Tecnai F30, FEI, USA) operated at 300 KV. The TEM specimens were first manually ground to approximately 40 μm and then twin-jet electropolished with a solution of 10 vol. % perchloric acid in methanol.

The nanotips for atom probe tomography (APT) were prepared in an FEI Scios focused ion beam/scanning electron microscope (FIB/SEM). APT was carried out in a CAMEACA LEAP 5000 XR system with a 200 kHz pulse repetition rate, 20% pulse fraction, and 0.2% atom per pulse evaporation detection rate at 70 K in voltage mode. The data analysis and three-dimensional reconstructions were performed using the Imago Visualization and Analysis Software (IVAS) version 3.8.

3. Results

3.1. Alloy design and material processing

The $CoCrNi_2(Al_{0.2}Nb_{0.2})$ alloy was designed using the Thermo-Cal software with the TTNI8 database (Fig. 1). The reasons for selecting this $CoCrNi_2(Al_{0.2}Nb_{0.2})$ alloy were as follows. A non-equiatomic $CoCrNi_2$ alloy with an increased Ni content can ensure that the elemental partitioning between the matrix and $L1_2$ phase which can *in situ* form a near-equiatomic CoCrNi matrix with low SFE and simultaneously produce a high density of $L1_2$ phase. We chose 4.5 at.% Al and 4.5 at.% Nb to form $L1_2$ nanoprecipitates without forming other intermetallic phases in the temperature range of 580-850 °C (Fig. 1). The increased precipitate/matrix lattice misfit, which can induce local lattice distortion and thereby offer resistance to dislocation motion, was achieved by adding Nb instead of Ti because of the intrinsically larger atomic size of Nb. In addition, Cr and Nb are well known as important alloying elements in Ni-based superalloys to enhance oxidation resistance and give high strength at elevated temperatures [34,35].

For the processing of the alloy, the aging temperature above 700 °C is adopted due to the slow diffusion of elements in $L1_2$- strengthened alloys [31,36]. This relatively high temperature allows the fast precipitation
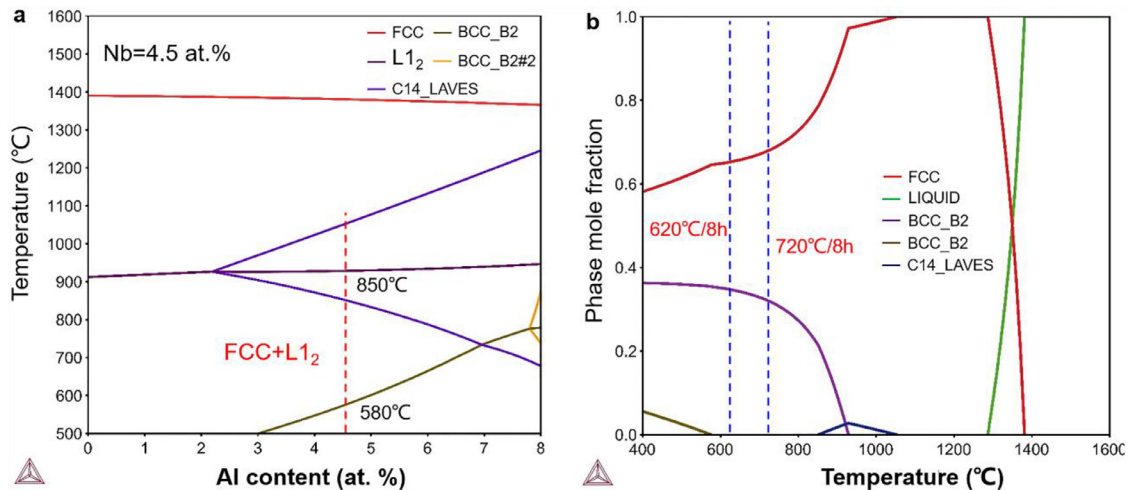
Fig. 1. Thermodynamic calculations of the $(CoCrNi_2)_{95.5-x}Al_xNb_{4.5}$ (at%) alloy system. (a) The calculated phase diagram from Thermo-Cal software with TTNI8 database. (b) The variations of equilibrium molar phases fraction with temperature.

of $L1_2$, but to prevent matrix grain coarsening, a duplex-aging process was used in this work to induce nanoscale $L1_2$ precipitation with an extremely high number density.

3.2. Phase and microstructure

The XRD pattern of the duplex-aged $CoCrNi_2(Al_{0.2}Nb_{0.2})$ alloy shows a single phase with the fcc structure (Fig. 2a). The lattice parameter was determined to be 3.581 Å by the extrapolation method [37]. The EBSD inverse pole figure (IPF) image (Fig. 2b) shows that the aged alloy was fully recrystallized, with a random grain orientation distribution and consisting of uniform equiaxed grains with an average size of ~40 μm (not including the annealing twins). Similar to a CoCrNi MEA [38], a large fraction of annealing twins suggests that the aged alloy has a low SFE. A representative bright-field TEM image (Fig. 2c) shows no precipitate segregation at the grain boundaries. A selected area electron diffraction (SAED) pattern obtained from the grain interior along the [001] zone axis shows the presence of superlattice diffraction spots. This indicates the formation of an $L1_2$ ordered phase within the disordered fcc matrix during the duplex-aging process. A typical dark-field TEM image (Fig. 2d) shows the presence of a high density of spherical nanoprecipitates (~12 nm) with a highly uniform distribution. High-resolution TEM was used to investigate the interfacial orientation between the nanoprecipitates and the fcc matrix. The fast Fourier transform (FFT) patterns (Fig. 2e) with [100] zone axis confirmed the presence of nanoprecipitates of an ordered $L1_2$ phase and a coherent interface between the nanoprecipitate and the matrix. Because the ordered $L1_2$ phase cannot be identified by XRD, the lattice parameters of the fcc matrix and the $L1_2$-type $Ni_3(Al, Nb)$ precipitated phase were determined to be 3.55 Å and 3.60 Å, respectively, from the high-resolution TEM images and corresponding inverse FFT images (Fig. S1), with a relatively large lattice mismatch of approximately 1.4%. Based on these results, a schematic diagram was constructed to illustrate the detailed microstructure of the aged alloy (Fig. 2f). It consists of a disordered fcc matrix with numerous annealing twins and a high density of coherent ordered $L1_2$-type nanoprecipitates.

Because of the extremely small size of these $L1_2$ precipitates, APT was used to reveal the composition, 3D morphology, and distribution of these nanoscale precipitates (Fig. 3). An APT reconstruction based on the 7% Nb iso-concentration surface was obtained to delineate the profile of the nanoprecipitates (Fig. 3a). The spherical precipitates are uniformly distributed in the matrix and the size of the precipitates is ~12 nm, which is consistent with the TEM observations. The elemen-

tal distribution (Fig. 3b) clearly shows elemental partitioning behavior, in which Ni, Al and Nb have strong tendency to partition into the nanoprecipitates, whereas Co is partially depleted and Cr is completely depleted in the nanoprecipitates. The proximity histogram for elemental partitioning across the interface between the precipitates and matrix (Fig. 3c) shows that all the elements have continuous transition between the fcc matrix and $L1_2$ precipitates, with a diffuse interface width of ~2 nm. The quantitative elemental compositions of the fcc matrix and $L1_2$ phase are summarized in Table S1. The precipitates are rich in Ni, Al and Nb, whereas the matrix has a near-equiatomic CoCrNi composition. In detail, the precipitates contain mainly Ni (~64.84 at.%), Co (~8.22 at.%), Al (~13.29 at.%), and Nb (~12.22 at.%). The matrix has an average composition of Co (~31.09 at.%), Cr (~34.97 at.%), Ni (~32.01 at.%), and a trace amount of Al (~0.66 at.%) and Nb (~1.26 at.%). The schematic diagram in Fig. 3d shows that the fcc matrix and nanoprecipitates can be identified as a near-equiatomic CoCrNi matrix and $(Ni, Co)_3(Al, Nb)$-type $L1_2$ phase, respectively. The volume fraction of the $L1_2$ phase was determined to be ~40% by using the lever rule (Fig. S2) [39,40].

3.3. Mechanical properties

The engineering tensile stress-strain curves of the aged alloy at room temperature were shown in Fig. 4a. To emphasize the substantial improvement after duplex-aging treatment, the curves of the as-cast and the solution-treated $CoCrNi_2(Al_{0.2}Nb_{0.2})$ alloy are also presented. The as-cast alloy has a relatively high yield strength (σ_y) of 653 MPa and a reasonable uniform elongation (ε_u) of 8.5%. The solution-treated alloy has a lower σ_y of 420 MPa with a ε_u of 30%. However, after duplex-aging, the alloy shows a tensile σ_y of up to 1150 MPa, an ultrahigh ultimate tensile strength (σ_{UTS}) of 1600 MPa and a ε_u of up to 33%. The aged alloy shows over 1 GPa increase in σ_{UTS}, but without ductility reduction compared to the solution-treated specimens. The aged alloy shows a simultaneous strength-ductility enhancement, evading the strength-ductility trade-off. The engineering stress-strain curve clearly shows superior plastic strain at such a high-strength level, accompanied by a superb strain hardening ability ($\sigma_{UTS}-\sigma_y = 450$ MPa).

The SHRs ($\theta = d\sigma/d\varepsilon$) of the three groups of alloys were determined from their corresponding true stress- true strain curves (Fig. 4b). After aging, the alloy was significantly strengthened due to the precipitation of the nanoscale $L1_2$ precipitates. Because of the formation of coherent $L1_2$ phase, the SHR of the aged alloy differs from those of the as-cast and the solution-treated alloys. The aged alloy has excellent strain harden-
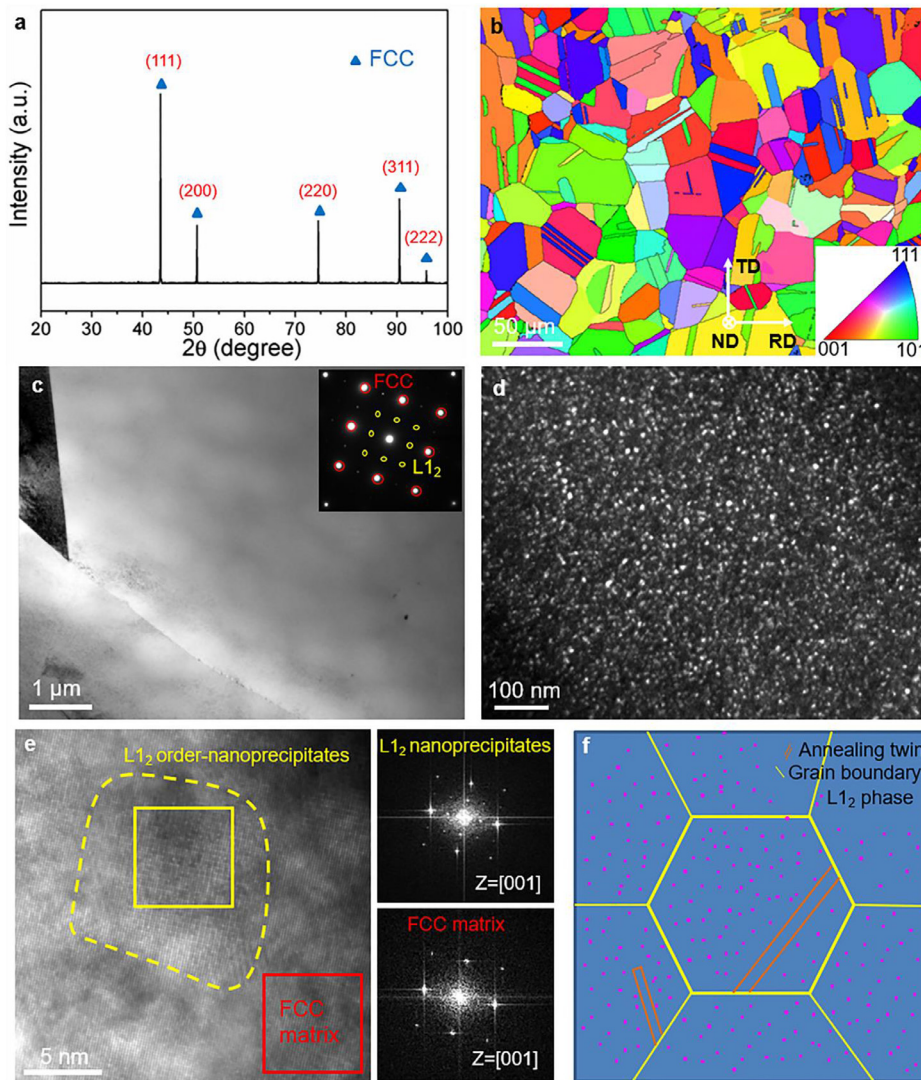
Fig. 2. The microstructure of the aged CoCrNi$_2$(Al$_{0.2}$Nb$_{0.2}$) alloy. (a) XRD pattern. (b) EBSD IPF map, where the directions normal to the rolling surface, the rolling direction and transverse direction in the rolling plane are defined as ND, RD and TD, respectively. (c) Bright-field TEM image with the inset of the SAED pattern showing the formation of L1$_2$ phase. (d) Dark-field TEM image showing the presence of a high-density L1$_2$-type nanoprecipitates. (e) A representative high-resolution TEM image with corresponding FFT patterns, showing the interfacial coherency between the fcc matrix and L1$_2$ nanoprecipitate. (f) Schematic diagram illustrates the microstructure of the aged alloy, consisting of a high number density L1$_2$-type nanoprecipitates and some annealing twins in the fcc matrix.

ing, resulting in a maximum true stress of 2139 MPa from an initial σ_y of 1150 MPa. Unlike those of the other two alloys, the strain hardening curve of the aged alloy shows multiple stage strain hardening behavior. There are three distinct deformation stages in strain hardening, as is often observed in TRIP/TWIP alloys [41]. Initially, the SHR decreases rapidly to a strain of 5.1%, at which the true stress reaches 1335 MPa (Stage I). This is followed by an increase to an ultrahigh value of 4 GPa at a strain around 18.8% (Stage II). In the Stage III, the SHR gradually decreases until fracture. Noted that even at the strain of ~30%, the SHR can reach ~2 GPa. This outstanding strain hardening considerably improves the strength and gives a large uniform elongation. These results indicate that the strain-hardening capacity of the current aged alloy is significantly enhanced due to the precipitation of the high density coherent L1$_2$ nanoprecipitates.

3.4. Fracture morphology

To reveal the deformed microstructure, we investigated the damage-evolution mechanisms and surface morphology by inspecting the fracture surfaces after tensile tests. The alloy surface was first polished

prior to straining. Fig. 5a shows that extensive microcracks are uniformly distributed near the fractured end and most of the cracks have long and tortuous morphology in addition to microvoids. The cracks are nearly perpendicular to the tensile direction. These cracks appear to be the primary cause of damage. Multiple slip steps are clearly observed, and significant interactions between slip steps occur within grains, which leads to the formation of deformation substructures (Fig. 5b-e).

The fracture morphology of the aged alloy shows no obvious macroscopic necking during tensile tests (Fig. 6a). A large number of dimples observed in Fig. 6b-d indicates a basic ductile fracture mode with fine dimples formed through the nucleation and coalescence of fine microvoids. However, flat facets with slip traces are also present, which give a quasi-cleavage appearance (Fig. 6c). The localized slip traces observed on the fracture surface do not immediately develop into cracks after nucleation because the adjacent dimpled region can release localized strain concentrations [42]. Such microstructure in the fractured specimens and fracture surface are similar to TWIP steel at liquid nitrogen temperature, which demonstrate better strength-ductility combination than that at room temperature [43].
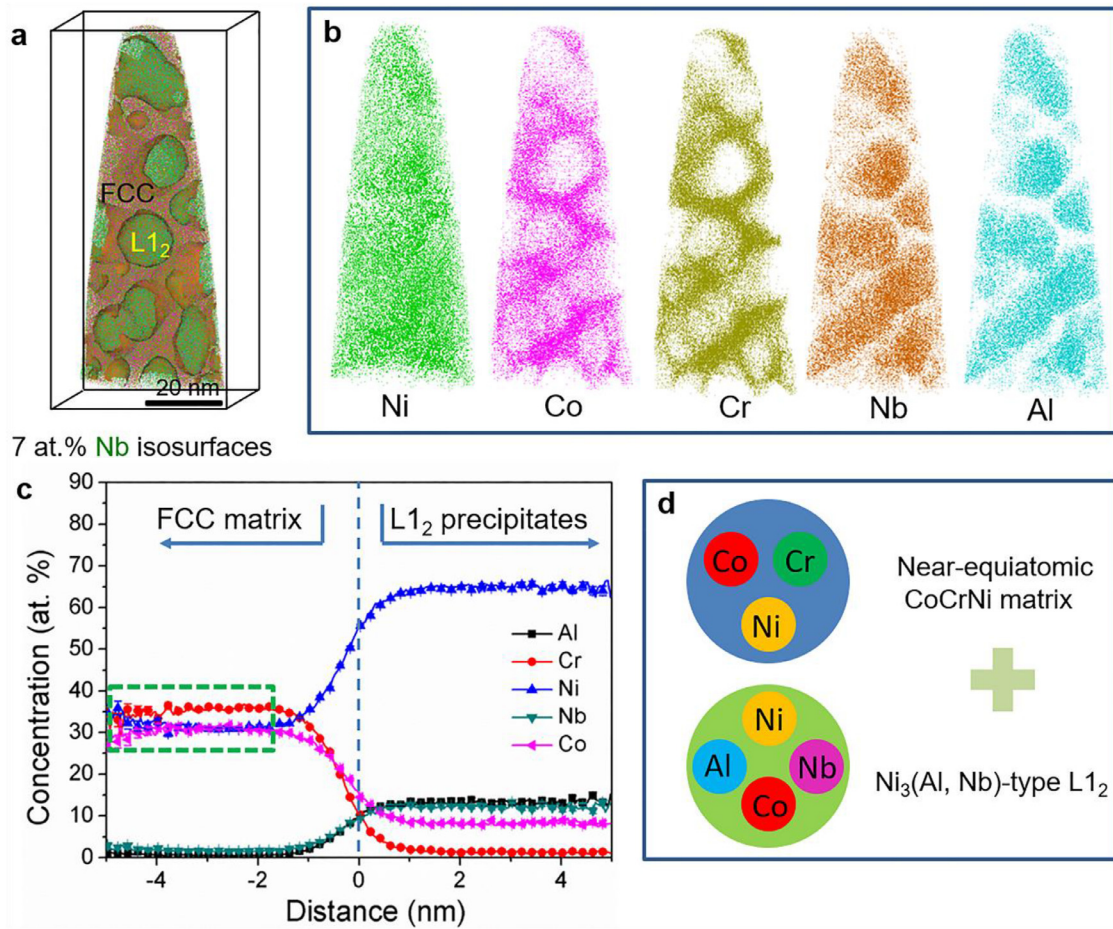
Fig. 3. Three-dimensional compositional distribution of the aged CoCrNi$_2$(Al$_{0.2}$Nb$_{0.2}$) alloy. (a) APT reconstruction in an analyzed space of 40 nm × 40 nm × 90 nm, showing the distribution of fcc matrix and L1$_2$ nanoprecipitates. (b) Atom maps of different elements. (c) Proximity histogram profile showing the compositional variation across the fcc matrix and L1$_2$ nanoprecipitates. (d) Schematic diagrams showing the elemental distribution of the fcc matrix and L1$_2$ nanoprecipitates in the aged alloy.
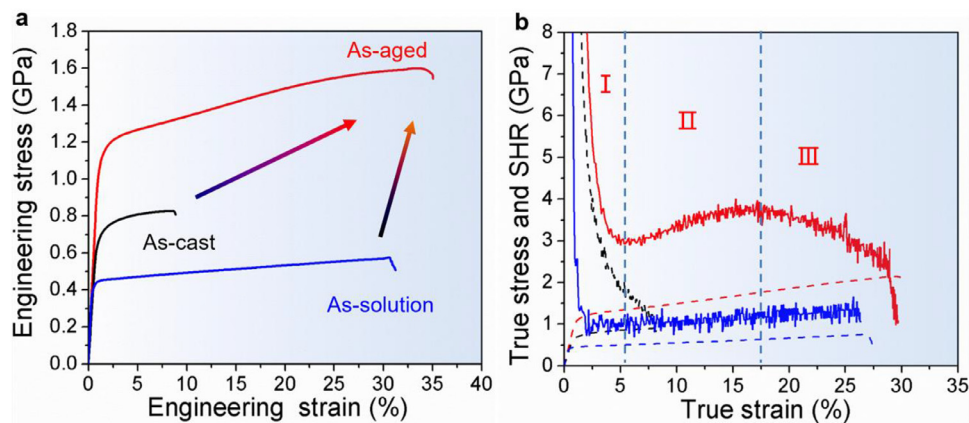

Fig. 4. Tensile properties of the CoCrNi$_2$(Al$_{0.2}$Nb$_{0.2}$) alloy. (a) Representative engineering stress-strain curves showing substantially enhancement in strength and ductility after cold-rolling and ageing. (b) The tensile true stress-true strain curves (dotted line) and corresponding strain-hardening rate versus true strain curves (solid line). The multistage stress-strain relationships are marked as stage I-III in the aged alloy.

4. Discussion

We used thermodynamic calculations to design a non-equiatomic CoCrNi$_2$(Al$_{0.2}$Nb$_{0.2}$) alloy. The aged alloy consists of an fcc matrix with a high density of coherent L1$_2$ nanoprecipitates (Fig. 2). This is consistent with the prediction of thermodynamic calculations (Fig. 1). The non-equiatomic CoCrNi$_2$(Al$_{0.2}$Nb$_{0.2}$) alloy shows outstanding tensile properties with σ_y and σ_{UTS} values of 1150 MPa and 1600 GPa, respectively,

at room temperature. The designed alloy also has an ultrahigh SHR, and gives a ε_u of 33% without any necking during tensile tests (Fig. 6).

4.1. Deformation mechanisms

We investigated the deformation mechanisms to explain the enhanced strength-ductility synergy in the aged alloy. The underlying mechanisms for the superior mechanical responses are discussed be-
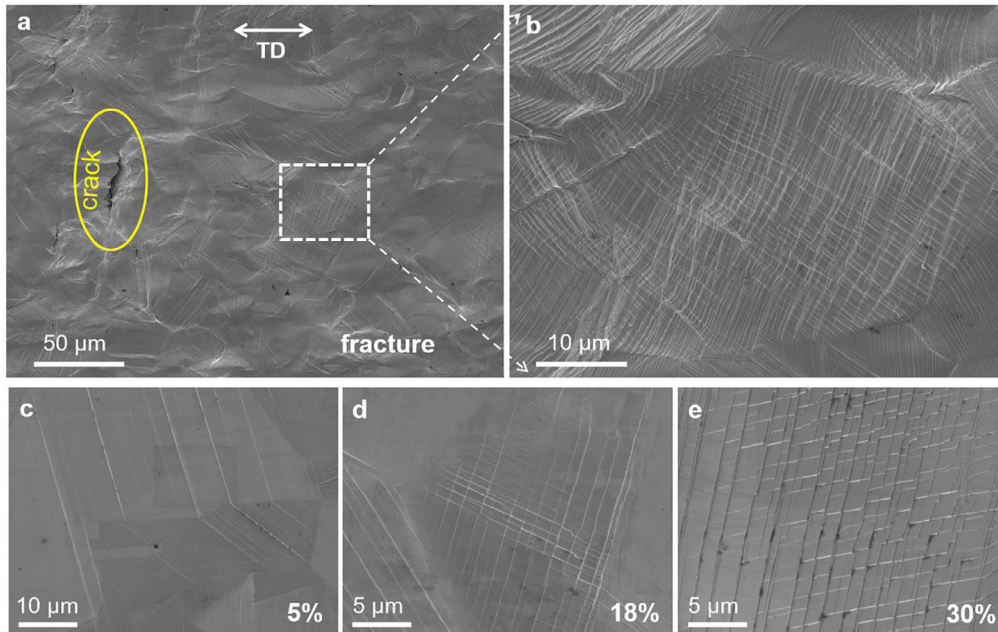
Fig. 5. Evolution of the surface microstructure during deformation. (a) Microcrack distribution near the fractured end. (b) A higher magnification SEM image of the dispersed slip bands. (c-e) SEM images of the deformed microstructure at varying strains.
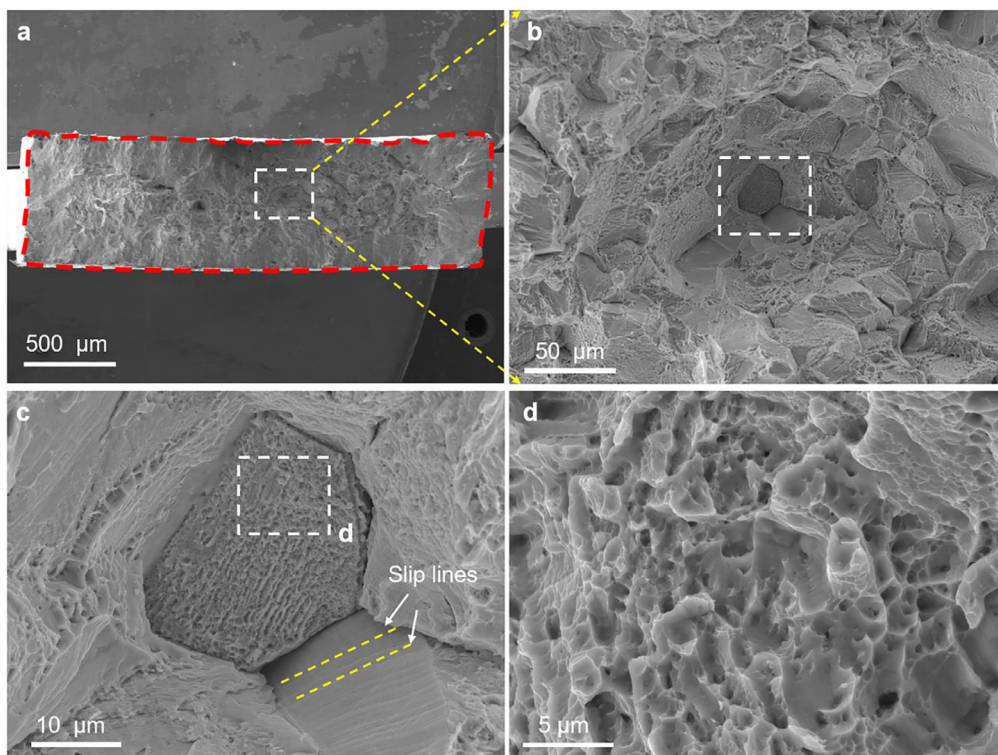

Fig. 6. SEM micrographs of the fracture surface at multiple length-scales. (a) The entire fracture surface of the tensile specimen showing the absence of necking during the tensile test. (b-c) Higher magnification SEM images of the representative fracture surface. The fracture surface mainly consists of dimples, feature of ductile fracture through the nucleation and coalescence of fine microvoids, and some quasi-cleavage appearance with flat facets. (d) High magnification SEM image of the dimples.

low. Fig. 7a-c displays EBSD IPF map, kernel average misorientation (KAM) map, and image quality map near the fracture surfaces of the aged CoCrNi$_2$(Al$_{0.2}$Nb$_{0.2}$) alloy after tensile tests. Deformation twinning is hardly detectable in these maps, presumably because of the small size and low volume fraction (Fig. 7a). The KAM image (Fig. 7b) shows an increase in local misorientations after deformation, which suggests a

higher number of geometrically necessary dislocations and pronounced dislocation activities after tensile deformation. Unindexed points in the image quality map (Fig. 7c) were notably present within the grains, which is morphologically consistent with twin boundaries or slip traces. The misorientation profile plotted in Fig. 7d reveals the presence of low angle grain boundaries, in line with stepwise increments in local misori-
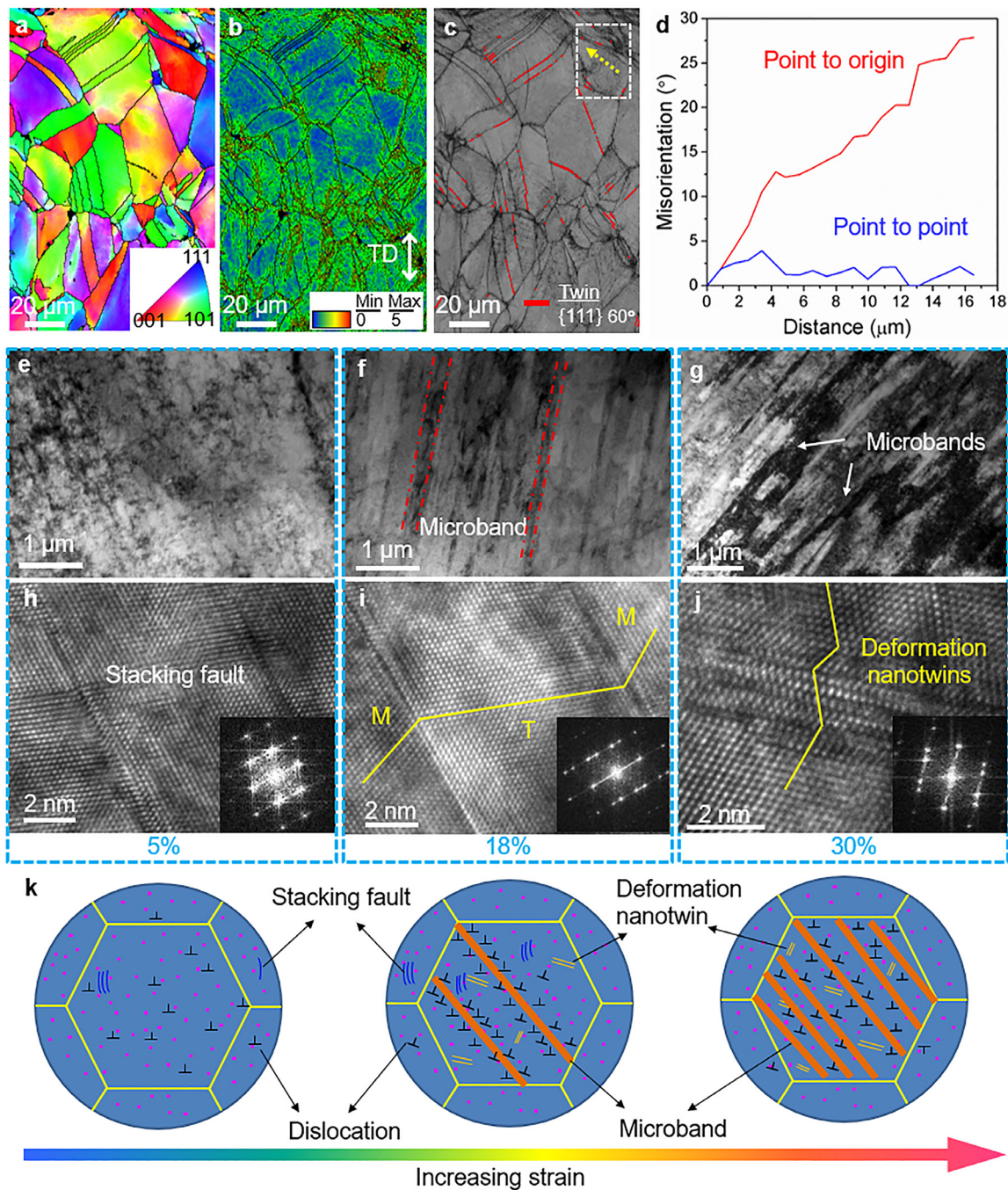
Fig. 7. Deformation mechanisms in the aged CoCrNi$_2$(Al$_{0.2}$Nb$_{0.2}$) alloy. (a-c) EBSD inverse pole figure, KAM, and image quality maps of the room-temperature tensile-fractured surface, respectively. (d) The corresponding plots of the misorientation variation across the yellow arrow marked in c. (e-g) Bright-field TEM images of the alloy with varying strains of 5%, 18%, and 30%, respectively, and the sample with the strain of 30% revealing the formation of microbands. (h-j) High-resolution TEM images for the alloy subjected to different strains revealing the formation of nanosized deformation twins. (k) Schematic illustration of the microstructure evolution during deformation.

entations. We also observed that the annealing twin boundaries acted as barriers to dislocation motion and thus contributed to strengthening (Fig. 8). This deformed microstructure indicates that planar arrays of high-density dislocations result in plastic accommodation and the strain hardening process.

The evolution of the deformed microstructures and the underlying mechanisms were further investigated by performing bright-field TEM and high-resolution TEM analyses of the deformed samples under various strains of 5%, 18%, and 30% (Fig. 7e-j). In the early deformation stage, under a strain of ~5%, the alloy has high-density dislocations homogeneously distributed inside the grains, which are deformed by typical planar slipping of dislocations on the {111} slip planes, similar to most fcc alloys [16,19,44]. The grains also have a low density of SFs, which indicates the onset of perfect dislocations divides into $a/6<112>$ partial dislocations (Fig. 7e, h). These observations show that the alloy starts to deform by dislocation gliding during stage I, which is in good agreement with the analysis of slip traces (Fig. 5). Hence, the SHR at this stage decreases as the gliding of dislocations. As the strain increased to 18%, microbands were observed, despite not being found in the EBSD analysis. Microbands originate from slip of dislocations, and the for-
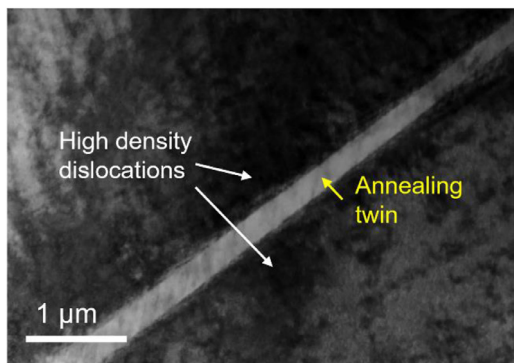
Fig. 8. High density dislocations around the annealing twin after deformation. The annealing twin can act as barriers to dislocation motion, thus improving the work hardening.

mation of microbands leads to the grain subdivision. The high-density dislocations in the microbands effectively decrease the mean free path of movable dislocations, and this produces stronger strain hardening as straining from 5% to 18%. Deformation twins with thicknesses in the order of tens of nanometers were observed. When the strain was further increased to 30%, intersection of well-developed microbands was observed. The presence of such parallel microbands at elevated stress results in the ultrahigh and sustained SHR. A similar microstructure was reported in (FeCoNi)$_{86}$Al$_8$Ti$_6$ alloy, and this is the main mechanism responsible for its high strength and ductility [16]. Deformation twins with a width of only a few nanometers were observed in high-resolution TEM image (Fig. 7g). These results show that the simultaneous formation of microband and nanotwins is mainly responsible for the ultrahigh SHR of this novel L1$_2$-strengthened MEA, as schematically shown in Fig. 7k. Therefore, MBIP and TWIP are the key mechanisms for the excellent ductility of this gigapascal-level alloy.

4.2. Formation of mechanical twins and microbands

Another deformation process, namely mechanical twinning, competes with dislocation slip. The SFE of fcc-structured alloys significantly affects the activation of plastic deformation modes, such as dislocation slip, mechanical twinning and phase transformation. The SFE therefore affects the strain hardening ability and consequently the mechanical properties of alloys. Typically, for fcc metals and alloys, a particular SFE range correlates with the dominant deformation mechanism. The critical SFE below which twinning occurs in fcc materials is ~45 mJ/m^2 [45]. It is assumed that the nucleation of twins occurs by dissociation of

an ($a/2$) <110> perfect dislocation into two ($a/6$) <112> Shockley partial dislocations. The formation of mechanical twinning is facilitated by stress concentrations to overcome the critical resolved shear stress for twinning (τ_{crss}). On the basis of the classical dislocation theory [46,47], the stress required to activate a Shockley partial twinning dislocation of length D is:

$$\tau_P = \gamma_{SF}/b_p + 2\alpha\mu b_p/D \tag{1}$$

and:

$$\tau_{crss} = \gamma_{SF}b_N/b_p(b_N - b_p) \tag{2}$$

where γ_{SF} is the SFE of CoCrNi (~22 ± 4 mJ/m^2, determined experimentally [24] or even a negative value, obtained from *ab initio* calculations [32,48]), μ is the shear modulus (87 GPa for CoCrNi [49]), α represents the type of dislocation (0.5 for edge dislocations), $b_N = (\sqrt{2}/2)a$ and $b_P = (\sqrt{6}/6)a$ are the Burgers vectors of the perfect dislocation and the Shockley partial dislocation, respectively. The calculated critical resolved shear stress τ_{crss} is 364 MPa and the stress required to activate a Shockley partial dislocation, τ_P, is calculated to be 998-2692 MPa for the CoCrNi matrix for a width range of 10-30 nm. In comparison with the flow stress of the present alloy, it is possible that mechanical twinning can be activated when the width of the CoCrNi matrix channel is appropriate because τ_{crss} and τ_P are readily reached in these regions.

Deformation-induced microbands have been observed in conventional metals and alloys, as well as in HEAs [15,18,19]. Microbands are characterized by local high-density dislocations, which are associated with a strain localization during deformation. Different from shear bands with a non-crystallographic alignment, microbands are usually aligned along the {111} slip planes. Planar slip is promoted by the constraints of dislocation movement caused by low SFE and the short-range order (SRO) [17]. And then the dislocations are arranged into parallel bands by the occurrence of planar slip, which can uniformly accommodate plastic deformation [18]. The present alloy showed the planar glide characteristics and no dislocation cell formation, even up to failure. Yoo *et al.* [18] reported microbands were observed in a Mn-Al-C steel with a relatively high SFE (~90 mJ/m^2). However, Huang *et al.* [50] demonstrated that the occurrence of microbands was not strongly dependent on the SFE, and microbands were also observed in alloys with relatively low SFE (10-20 mJ/m^2) [26]. In the present study, the CoCrNi matrix with low SFE does not affect the formation of microbands. The large atomic size of Nb generates larger local lattice distortions, leading to higher lattice friction stress (σ_i) as dislocations pass through the lattice. The increase in friction stress due to the Nb solute in our alloy hinders the formation of dislocation cells, and further promotes microband formation [26]. Deformation-induced microbands are involved in an im-
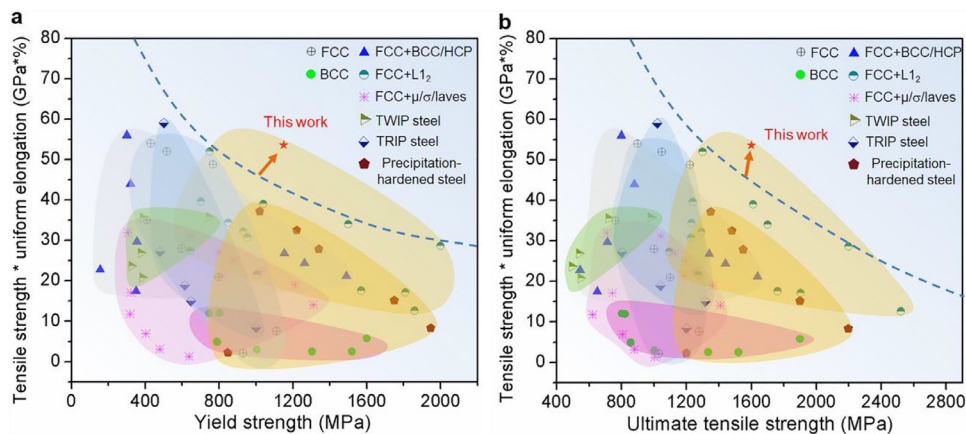

Fig. 9. Comparisons in tensile properties of our CoCrNi$_2$(Al$_{0.2}$Nb$_{0.2}$) alloy with other previously-reported HEAs and other high-performance steels. The specific data of the tensile properties are presented in Table S2.
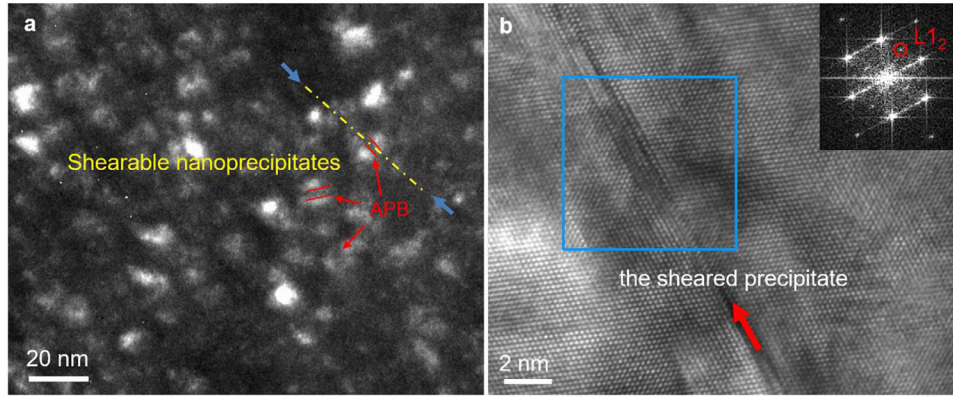
Fig. 10. The interaction between L1$_2$ nanoprecipitates and dislocations. (a) Dark-field TEM image of the CoCrNi$_2$(Al$_{0.2}$Nb$_{0.2}$) alloy showing the sheared L1$_2$ nanoprecipitates by gliding dislocations. (b) High-resolution TEM image indicates the shear of L1$_2$ precipitate.

portant ductilizing mechanism, namely the so-called MBIP, which produces similar strain hardening effects to those caused by TWIP and TRIP. A large strain hardening ability can delay the occurrence of necking during tensile deformation, and this leads to enhanced ductility. In addition, these dislocation substructures can induce the grain subdivision and refinement, which further enhance the strength due to the dynamic Hall-Petch effect.

We found that this compositional modification caused by elemental partitioning from the precipitation reaction of Ni$_3$(Al, Nb)-type L1$_2$ decreased the SFE of the fcc matrix in our aged alloy. In other Al-bearing fcc HEAs [51,52], it is also found that the SFEs of materials decrease by reducing the Al concentrations. This promotes extensive twinning deformation and even phase transformation. In the present study, similarly, we decreased the local SFE in our alloy by forming a near-equiatomic CoCrNi matrix, as confirmed by APT analysis. Consequently, the dissociation of perfect dislocations for twinning was promoted due to the reduced local SFE. When the true strain was increased to overcome τ_P, nanotwin formation gradually occurred. The dynamic nanotwin-dislocation interactions can be stimulated, resulting in appreciable strain hardening and uniform elongation [21]. The high-density dislocations in the microbands can significantly decrease the mean free path of dislocation, and dislocation slip on parallel microbands is also increasingly hindered as the microband spacing becomes finer under higher stress (Fig. 7g). The absence of cross slip can effectively impede dynamic recovery and promote massive dislocation accumulation, which can lead to a larger SHR in dynamic [53,54]. The detected large tensile ductility is therefore primarily caused by the unusual nanotwin-microband structure in our alloy, which can contribute to higher strain hardening and strength-ductility synergy than those observed for other L1$_2$-strengthened HEAs.

The outstanding mechanical properties of this alloy were demonstrated by comparison with previously-reported HEAs and other high-performance steels (Fig. 9). The tensile properties of various alloys are closely related to the phases in the alloys. Generally, fcc alloys have good ductility but relatively low strength, while bcc alloys are strong but low ductility, and the multiphase alloys have better strength-ductility combinations than single-phase ones. In particular, L1$_2$ strengthened-HEAs are very attractive among the multiphase alloys. The present alloy shows an apparent advantage over existing bulk HEAs, namely a high σ_y and σ_{UTS}, and a good strength-ductility combination. It therefore has a great potential for extreme structural applications. Several factors contribute to the superior tensile properties of this alloy. Firstly, a high number density of nanoscale coherent spherical precipitates can strongly hinder the dislocation motion by providing obstacles in trapping moving dislocations, and by generating anti-phase boundaries on the slip planes of these nanoprecipitates. These can enhance the plas-

tic deformation stability and achieve an ultrahigh strength (Fig. 10). Secondly, the intrinsically low SFE of the fcc matrix promotes the formation of microband-nanotwin structures under tensile strain, which significantly improves the strain-hardening capacity and leads to superior tensile ductility, even at ultrahigh strength levels. Thirdly, the large atomic size of Nb can increase the local lattice distortion, which can lead to higher σ_i when dislocations pass through the material. Moreover, the dedicated composition design endows the present CoCrNi$_2$(Al$_{0.2}$Nb$_{0.2}$) alloy with advantages over other existing high strength alloys. For example, Nb addition gives the materials superior high-temperature properties, which makes them potentially attractive for aerospace and aeronautic applications.

4.3. Estimation of strengthening mechanisms

The present CoCrNi$_2$(Al$_{0.2}$Nb$_{0.2}$) alloy shows outstanding tensile properties with an ultrahigh σ_y of 1150 MPa and σ_{UTS} of 1600 MPa at room temperature after a duplex-aging process. The microstructural characterizations indicate that potential strengthening mechanisms should involve a combination of solid solution strengthening $\Delta\sigma_s$, grain size strengthening ($\Delta\sigma_g$), precipitation strengthening $\Delta\sigma_p$, and the lattice friction strength σ_i. Residual dislocations have been completely eliminated in the alloy after the recrystallization and the final aging, therefore dislocation strengthening can be ignored. The yield strength of the alloy can therefore be expressed as:

$$\sigma_y = \sigma_i + \Delta\sigma_s + \Delta\sigma_g + \Delta\sigma_p \tag{1}$$

For HEA/MEAs, it is difficult to evaluate the strengthening by solute atoms due to the distinguishable solvent and solute. However, for a given system, solution strengthening and the lattice friction strength should be similar, and therefore the change in the strength of the annealed alloy can be attributed to variations in grain size. As a result, the intercept term σ_0 in the Hall-Petch equation ($\Delta\sigma_g = \sigma_0 + k_g \cdot d^{-1/2}$, where d is the average grain size and k_g is the Hall-Petch coefficient) can be considered as a constant, which consisted of the solution strengthening $\Delta\sigma_{ss}$ and lattice friction stress σ_i:

$$\sigma_0 = \sigma_i + \Delta\sigma_{ss} \tag{2}$$

By this consideration, the estimation of the lattice friction strength and solution strengthening can be reasonably simplified in the alloy:

$$\Delta\sigma_{gs} = k_g d^{-1/2} \tag{3}$$

In order to acquire grains of different sizes, the cold-rolled samples were annealed at 1100 °C for various holding times (10, 30, 90, and 180 min). The relationship between tensile properties and grain sizes of these as-annealed samples is determined (Fig. 11). The intercept term
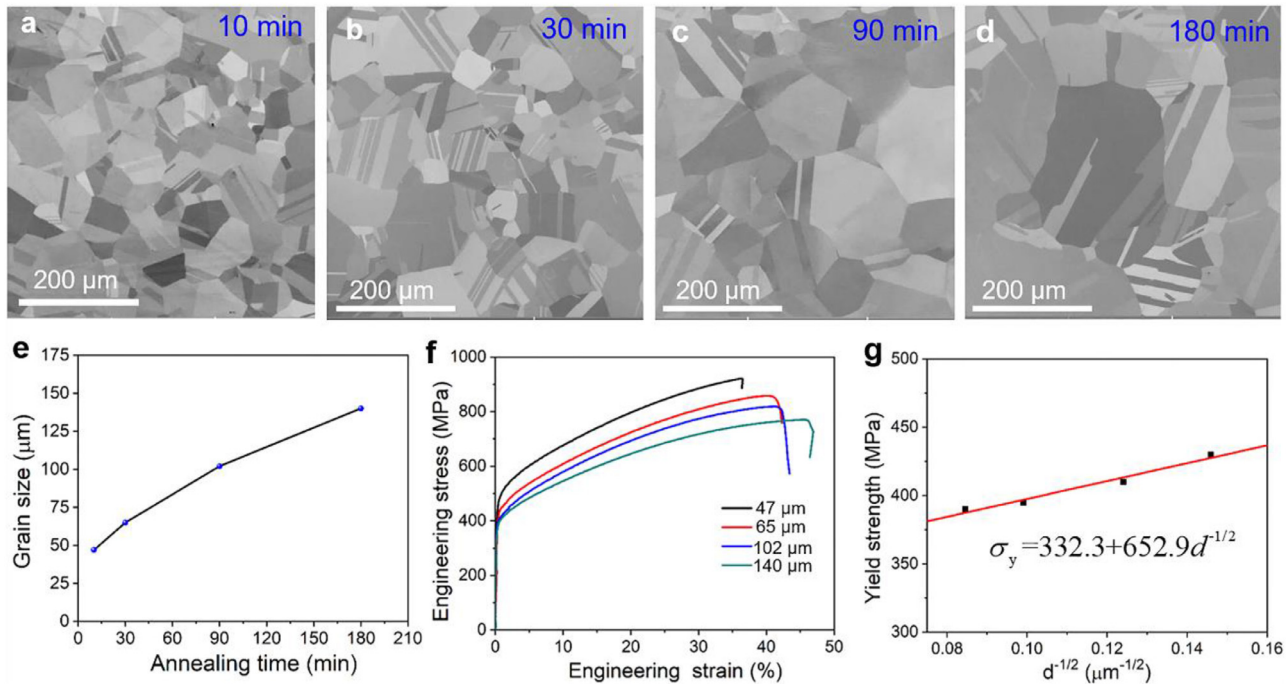
Fig. 11. Grain structure and tensile properties of CoCrNi$_2$(Al$_{0.2}$Nb$_{0.2}$) alloy annealed at 1100 °C for different times. (a-d) SEM images of the CoCrNi$_2$(Al$_{0.2}$Nb$_{0.2}$) alloy annealed at different times. (e) The variation of grain size as a function of annealing time. (f) Tensile engineering stress-strain curves of the CoCrNi$_2$(Al$_{0.2}$Nb$_{0.2}$) alloys with various grain sizes at room temperature. (g) Plots of yield strength versus inverse square root of grain size of the CoCrNi$_2$(Al$_{0.2}$Nb$_{0.2}$) alloy.

σ_0 and Hall-Petch coefficient k_g, were obtained as $\sigma_0 = 332.3$ MPa and $k_g = 652.9$ from Fig. 11g. The grain boundary contribution to the yield strengths is therefore 103 MPa.

For alloys containing a high number density of nanoprecipitates, precipitation hardening is primarily responsible for the pronounced increase in the yield strength. Due to the near fully coherent relationship of fcc/L1$_2$, the precipitation strengthening L1$_2$ phase is substantially sheared by gliding dislocations during deformation (Fig. 10). The strengthening contribution of the L1$_2$ phase ($\Delta\sigma_p$) therefore comes from order strengthening ($\Delta\sigma_{OS}$). The yield strength increase from $\Delta\sigma_{OS}$ can be estimated as [55]:

$$\Delta\sigma_{OS} = 0.81 M \frac{\gamma_{APB}}{2b} \left(\frac{3\pi f}{8}\right)^{\frac{1}{2}} \tag{4}$$

where the Taylor factor $M = 3.06$ is a constant for a polycrystalline fcc structure, b is the Burgers vector ($b = 0.2513$ nm), $f = 0.4$ is the volume fraction of the precipitates, and γ_{APB} is the anti-phase boundary energy of the nanoprecipitates (0.20 J/m^{-2}, obtained from Ni$_3$(Al,Ti) in Ni-based superalloys [56]). Accordingly, $\Delta\sigma_{OS}$ is calculated to be 677 MPa, which contributes the majority of the total yield strength. The total calculated yield strength of 1112 MPa agrees well with the experimental value of 1150 MPa.

5. Conclusion

In this work, guided by thermodynamic calculations and through the thermo-mechanical processing, we have designed and fabricated a CoCrNi$_2$(Al$_{0.2}$Nb$_{0.2}$) superlattice alloy by tailoring the chemical composition of the fcc matrix to control the local SFE. This compositional tuning promotes phase separation and generates a high number density of coherent L1$_2$ nanoprecipitates in the *in situ* formed near-equiatomic low SFE matrix. This alloy achieved a superior strength-ductility combination with σ_y of up to 1150 MPa and ε_u of 33%. The low SFE CoCrNi matrix provides a platform for forming deformation induced microband-nanotwin structures during tensile tests, which contributes to the superior strain hardening and tensile strength. Moreover, such a particular structure provides large plasticity via the synergetic mechanisms of microband and twinning induced plasticity. Our design strategy is based on tuning the initial compositions (non-equiatomic) to *in situ* form a near-equiatomic low SFE matrix after precipitating sufficient nanoprecipitates. Our work therefore provides a basis for designing alloys with unusual combinations of high strength and large ductility.

Declaration of competing interest

The authors declare that they have no conflicts of interest in this work.

Supplementary materials

Supplementary material associated with this article can be found, in the online version, at doi:10.1016/j.fmre.2022.05.024.

References

[1] R.O. Ritchie, The conflicts between strength and toughness, Nat. Mater. 10 (2011) 817–822.

[2] Y. Wang, M. Chen, F. Zhou, et al., High tensile ductility in a nanostructured metal, Nature 419 (2002) 912–915.

[3] X. Wu, M. Yang, F. Yuan, et al., Heterogeneous lamella structure unites ultrafine–grain strength with coarse-grain ductility, Proc. Natl. Acad. Sci. U. S. A 112 (2015) 14501–14505.

[4] K. Lu, Making strong nanomaterials ductile with gradients, Science 345 (2014) 1455–1456.

[5] E. Ma, T. Zhu, Towards strength-ductility synergy through the design of heterogeneous nanostructures in metals, Mater. Today 20 (2017) 323–331.

[6] B. Gwalani, S. Dasari, A. Sharma, et al., High density of strong yet deformable intermetallic nanorods leads to an excellent room temperature strength-ductility combination in a high entropy Alloy, Acta Mater. 219 (2021) 1–14.

[7] J.W. Yeh, S.K. Chen, S.J. Lin, et al., Nanostructured High-Entropy Alloys with Multiple Principal Elements:Novel Alloy Design Concepts and Outcomes, Adv. Eng. Mater. 6 (2004) 299–303.

[8] D.B. Miracle, O.N. Senkov, A critical review of high entropy alloys and related concepts, Acta Mater. 122 (2017) 448–511.

[9] E.P. George, D. Raabe, R.O. Ritchie, High-entropy alloys, Nat. Rev. Mater. 4 (2019) 515–534.

[10] Z. Li, S. Zhao, R.O. Ritchie, et al., Mechanical properties of high-entropy alloys with emphasis on face-centered cubic alloys, Prog. Mater. Sci. 102 (2019) 296–345.

[11] F. Otto, A. Dlouhý, C. Somsen, et al., The influences of temperature and microstructure on the tensile properties of a CoCrFeMnNi high-entropy alloy, Acta Mater. 61 (2013) 5743–5755.

[12] B. Gludovatz, A. Hohenwarter, D. Catoor, et al., A fracture-resistant high-entropy alloy for cryogenic applications, Science 345 (2014) 1153–1158.

[13] Z. Li, K.G. Pradeep, Y. Deng, et al., Metastable high-entropy dual-phase alloys overcome the strength-ductility trade-off, Nature 534 (2016) 227–230.

[14] Y. Deng, C.C. Tasan, K.G. Pradeep, et al., Design of a twinning-induced plasticity high entropy alloy, Acta Mater. 94 (2015) 124–133.

[15] Z. Wang, H. Bei, I. Baker, Microband induced plasticity and the temperature dependence of the mechanical properties of a carbon-doped FeNiMnAlCr high entropy alloy, Mater. Charact. 139 (2018) 373–381.

[16] T. Yang, Y.L. Zhao, Y. Tong, et al., Multicomponent intermetallic nanoparticles and superb mechanical behaviors of complex alloys, Science 362 (2018) 933–937.

[17] V. Yamakov, D. Wolf, S.R. Phillpot, et al., Deformation-mechanism map for nanocrystalline metals by molecular-dynamics simulation, Nat. Mater. 3 (2004) 43–47.

[18] J.D. Yoo, K.T. Park, Microband-induced plasticity in a high Mn-Al-C light steel, Mater. Sci. Eng. A 496 (2008) 417–424.

[19] I. Gutierrez-Urrutia, D. Raabe, Multistage strain hardening through dislocation substructure and twinning in a high strength and ductile weight-reduced Fe-Mn-Al-C steel, Acta Mater. 60 (2012) 5791–5802.

[20] E. Welsch, D. Ponge, S.M. Hafez Haghighat, et al., Strain hardening by dynamic slip band refinement in a high-Mn lightweight steel, Acta Mater. 116 (2016) 188–199.

[21] G. Laplanche, A. Kostka, O.M. Horst, et al., Microstructure evolution and critical stress for twinning in the CrMnFeCoNi high-entropy alloy, Acta Mater 118 (2016) 152–163.

[22] Y.T. Zhu, X.Z. Liao, S.G. Srinivasan, et al., Nucleation and growth of deformation twins in nanocrystalline aluminum, Appl. Phys. Lett. 85 (2004) 5049–5051.

[23] Z. Zhang, H. Sheng, Z. Wang, et al., Dislocation mechanisms and 3D twin architectures generate exceptional strength-ductility-toughness combination in CrCoNi medium-entropy alloy, Nat. Commun. 8 (2017) 1–8.

[24] G. Laplanche, A. Kostka, C. Reinhart, et al., Reasons for the superior mechanical properties of medium-entropy CrCoNi compared to high-entropy CrMnFeCoNi, Acta Mater. 292 (2017) 292–303.

[25] F. Otto, A. Dlouhy, Ch. Somsen, et al., The influences of temperature and microstructure on the tensile properties of a CoCrFeMnNi high-entropy alloy, Acta Mater. 61 (2013) 5743–5755.

[26] Z. Wang, I. Baker, Z. Cai, et al., The effect of interstitial carbon on the mechanical properties and dislocation substructure evolution in $Fe_{40.4}Ni_{11.3}Mn_{34.8}Al_{7.5}Cr_6$ high entropy alloys, Acta Mater. 120 (2016) 228–239.

[27] Y.L. Zhao, T. Yang, Y. Tong, et al., Heterogeneous precipitation behavior and stacking-fault-mediated deformation in a CoCrNi-based medium-entropy alloy, Acta Mater. 138 (2017) 72–82.

[28] J.Y. He, H. Wang, H.L. Huang, et al., A precipitation-hardened high-entropy alloy with outstanding tensile properties, Acta Mater. 102 (2016) 187–196.

[29] Y.L. Zhao, T. Yang, Y.R. Li, et al., Superior high-temperature properties and deformation-induced planar faults in a novel $L1_2$-strengthened high-entropy alloy, Acta Mater. 188 (2020) 517–527.

[30] Y.J. Liang, L. Wang, Y. Wen, et al., High-content ductile coherent nanoprecipitates achieve ultrastrong high-entropy alloys, Nat. Commun. 9 (2018) 1–8.

[31] Y. Tong, D. Chen, B. Han, et al., Outstanding tensile properties of a precipitation-strengthened $FeCoNiCrTi_{0.2}$ high-entropy alloy at room and cryogenic temperatures, Acta Mater. 165 (2019) 228–240.

[32] J. Ding, Q. Yu, M. Asta, et al., Tunable stacking fault energies by tailoring local chemical order in CrCoNi medium-entropy alloys, Proc. Natl. Acad. Sci. U. S. A 115 (2018) 8919–8924.

[33] T.M. Smith, M.S. Hooshmand, B.D. Esser, et al., Atomic-scale characterization and modeling of 60° dislocations in a high-entropy alloy, Acta Mater. 110 (2016) 352–363.

[34] J.Y. Chen, Q. Feng, L.M. Cao, et al., Improvement of stress-rupture property by Cr addition in Ni-based single crystal superalloys, Mater. Sci. Eng. A 528 (2011) 3791–3798.

[35] F. Weng, H. Yu, K. Wan, et al., The influence of Nb on hot corrosion behavior of Ni-based superalloy at 800°C in a mixture of Na_2SO_4-NaCl, J. Mater. Res. 29 (2014) 2596–2603.

[36] D.J. Sauza, D.C. Dunand, R.D. Noebe, et al., γ'-$(L1_2)$ precipitate evolution during isothermal aging of a Co-Al-W-Ni superalloy, Acta Mater. 164 (2019) 654–662.

[37] J.B. Nelson, D.P. Riley, An experimental investigation of extrapolation methods in the derivation of accurate unit-cell dimensions of crystals, Proc. Phys. Soc. 57 (1945) 160–177.

[38] C.E. Slone, S. Chakraborty, J. Miao, et al., Influence of deformation induced nanoscale twinning and FCC-HCP transformation on hardening and texture development in medium-entropy CrCoNi alloy, Acta Mater. 158 (2018) 38–52.

[39] I. Povstugar, P. Choi, S. Neumeier, et al., Elemental partitioning and mechanical properties of Ti- and Ta-containing Co-Al-W-base superalloys studied by atom probe tomography and nanoindentation, Acta Mater. 78 (2014) 78–85.

[40] Z. Wang, W. Lu, H. Zhao, et al., Formation mechanism of κ-carbides and deformation behavior in Si-alloyed FeMnAlC lightweight steels, Acta Mater. 198 (2020) 258–270.

[41] Y. Fu, W. Xiao, D. Kent, et al., Ultrahigh strain hardening in a transformation-induced plasticity and twinning-induced plasticity titanium alloy, Scr. Mater. 187 (2020) 285–290.

[42] P.-J. Yang, Q.-J. Li, W.-Z. Han, et al., Designing solid solution hardening to retain uniform ductility while quadrupling yield strength, Acta Mater. 179 (2019) 107–118.

[43] Y. Li, Y. Lu, W. Li, et al., Hierarchical microstructure design of a bimodal grained twinning-induced plasticity steel with excellent cryogenic mechanical properties, Acta Mater. 158 (2018) 79–94.

[44] B. Gludovatz, A. Hohenwarter, K.V. Thurston, et al., Exceptional damage-tolerance of a medium-entropy alloy CrCoNi at cryogenic temperatures, Nat. Commun. 7 (2016) 1–8.

[45] S. Curtze, V.T. Kuokkala, Dependence of tensile deformation behavior of TWIP steels on stacking fault energy, temperature and strain rate, Acta Mater. 58 (2010) 5129–5141.

[46] K.P.D. Lagerlöf, J. Castaing, P. Pirouz, et al., Nucleation and growth of deformation twins: A perspective based on the double-cross-slip mechanism of deformation twinning, Philos. Mag. 82 (2002) 2841–2854.

[47] J.A. Venables, Deformation twinning in face-centred cubic metals, Philos. Mag. 6 (1961) 379–396.

[48] S. Zhao, G.M. Stocks, Y. Zhang, Stacking fault energies of face-centered cubic concentrated solid solution alloys, Acta Mater. 134 (2017) 334–345.

[49] Z. Wu, H. Bei, G.M. Pharr, et al., Temperature dependence of the mechanical properties of equiatomic solid solution alloys with face-centered cubic crystal structures, Acta Mater. 81 (2014) 428–441.

[50] J.C. Huang, G.T. Gray, Microband formation in shock-loaded and quasi-statically deformed metals, Acta Metall. 37 (1989) 3335–3347.

[51] T. Cao, J. Shang, J. Zhao, et al., The influence of Al elements on the structure and the creep behavior of $Al_xCoCrFeNi$ high entropy alloys, Mater. Lett. 164 (2016) 344–347.

[52] X. Sun, H. Zhang, W. Li, et al., Generalized stacking fault energy of Al-doped CrMnFeCoNi high-entropy alloy, Nanomaterials 10 (2019) 1–8.

[53] K. Jiang, T. Ren, G. Shan, et al., Dynamic mechanical responses of the $Al_{0.1}CoCrFeNi$ high entropy alloy at cryogenic temperature, Mater. Sci. Eng. A 797 (2020) 1–9.

[54] X.D. Xu, P. Liu, Z. Tang, et al., Transmission electron microscopy characterization of dislocation structure in a face-centered cubic high-entropy alloy $Al_{0.1}CoCrFeNi$, Acta Mater. 144 (2018) 107–115.

[55] A.J. Ardell, Precipitation Hardening, Metall. Mater. Trans. A 16A (1985) 2131–2165.

[56] R.W. Kozar, A. Suzuki, W.W. Milligan, et al., Strengthening mechanisms in polycrystalline multimodal nickel-Base superalloys, Metall. Mater. Trans. A 40 (2009) 1588–1603.

Yang Lu is currently a Ph.D. student in the department of Materials Science and Engineering, Southern University of Science and Technology. He received the M. S. and B. S. degree from South China University of Technology and Jiangsu University, respectively. His research interests focus on mechanical properties and sliding wear behavior of medium/high-entropy alloy.

Fuzeng Ren (BRID: 03933.00.09629) is a tenured Associate Professor at the Department of Materials Science and Engineering, Southern University of Science and Technology (SUSTech). He received his Ph.D. and M.Phil. degree in Mechanical Engineering from Hong Kong University of Science and Technology. Before joining SUSTech as a faculty member, he worked as a Postdoctoral Research Associate in University of Illinois at Urbana-Champaign for three years. His research interest includes wear-resistant alloys and metallic biomaterials for orthopedic implants. He has published over 100 SCI papers and received National Science Fund for Excellent Young Scholars.